Carbohydrate Polymers 366 (2025) 123874

Contents lists available at ScienceDirect

Carbohydrate Polymers

journal homepage: www.elsevier.com/locate/carbpol

Distinct morphology and self-assembly behavior of Xylan nanoparticles are correlated with arabinose side-chains in Sorghum

Youmei Wang [a,1], Yaoyao Zhu [a,1], Min Li [a,c], Bingyi Ji [a], Shisheng Liu [a], Weiqing Liu [a], Zhen Hu [a], Hui Zhang [b], Wei Zhang [a], Liangcai Peng [d], Zhaosheng Kong [a,*]

[a] Shanxi Hou Ji Laboratory, College of Agriculture, Shanxi Agricultural University, Taiyuan, China
[b] College of Science, Shanxi Agricultural University, Taigu, China
[c] College of Grassland Science, Shanxi Agricultural University, Taigu, China
[d] Key Laboratory of Fermentation Engineering (Ministry of Education), Hubei Key Laboratory of Industrial Microbiology, School of Life and Health Sciences, Hubei University of Technology, Wuhan 430068, China

ARTICLE INFO

Keywords:
Sorghum
Arabinoxylan
Nanoparticles
Chiral self-assembly
Birefringent

ABSTRACT

Arabinoxylans (AXs) are complex polysaccharides with varying arabinose substitution patterns that affect their structural properties and self-assembly behaviors. In this study, we selected two sorghum varieties (S2 and S13) from a pool of 18 representative varieties, based on their distinct hemicellulose compositions. Techniques such as arabinoxylan-directed monoclonal antibodies (mAbs), High-Performance Anion-Exchange Chromatography (HPAEC), and 2-D HSQC NMR showed that S13 hemicellulose was of higher Ara/Xyl ratio of 0.22, compared to 0.09 in S2, which should be accounting for relatively high and low branching degrees of xylans. To gain deeper insights into the influence of arabinose side chains on xylan macromolecules, we measured and compared the morphology and self-assembly behaviors of nanoparticles from both varieties. Our findings indicate that nanoparticles from S2 were more slender and tended to assemble in a parallel orientation, while those from S13 displayed a vertical or disordered arrangement. By employing confined evaporation-induced self-assembly (C-EISA), we explored the self-assembly behavior of nanoparticles from each variety, and S13 nanoparticles in particular exhibited greater branching and distinct helical structures. These findings thus extend our understanding of the relationship between hemicellulose structure and its functional applications, offering insight for developing novel materials for drug delivery, biosensors, and other emerging applications.

1. Introduction

Polysaccharides comprise over 90 % of the carbohydrate mass present in nature, making them an invaluable resource for the development of sustainable materials (Liu et al., 2025; Ma et al., 2024). In the realm of nanomaterials, extensive exploration over the past few decades has focused on nanocrystals derived from natural polysaccharides, such as cellulose, chitin and starch (Si et al., 2021; Zhang, Hu, et al., 2023). These nanocrystals have been widely applied in various advanced functional materials, including biomimetic composites, drug carriers, biological scaffolds, and biosensors (Liao et al., 2023; Ling et al., 2021; Maingret et al., 2020; Sergeev et al., 2022; Wu et al., 2018; Xue et al., 2022; Zhang et al., 2021). Hemicellulose, as one of the natural polysaccharides, constitutes about 15 % to 38 % of the total weight of lignocellulosic biomass (Wang et al., 2016; Wang et al., 2021). It is generally regarded as amorphous due to the presence of side groups (Qaseem et al., 2021). Consequently, its proposed applications have primarily focused on bulk uses, such as films for packaging and coating (Liao et al., 2024; Liu et al., 2023; Naidu et al., 2018). The challenge of constructing controlled nanosized crystalline structures, such as rods or fibrils, from hemicellulose has significantly hindered its utilization in more complex material applications. Recently, research has begun to explore hemicellulose from the perspective of nanoparticles (Gericke et al., 2021; Smith et al., 2022; Zhang, Johnson, et al., 2023), however, due to its amorphous and complex structure, studies on the controlled size and morphology of nanocrystals remain limited.

Xylan is the most abundant hemicellulosic polysaccharide in the cell wall of grasses and features a backbone composed of β-1,4-linked D-

* Corresponding author.
E-mail address: zskong@sxau.edu.cn (Z. Kong).
[1] These authors contributed equally to this work

https://doi.org/10.1016/j.carbpol.2025.123874
Received 8 February 2025; Received in revised form 30 May 2025; Accepted 5 June 2025
Available online 6 June 2025

xylopyranosyl residues (Rennie & Scheller, 2014). Depending on the source of the raw material, xylan can be classified into three main types: arabinoxylan (AX), glucuronoxylan (GX), and glucuronoarabinoxylan (GAX) (Qaseem et al., 2024). Additionally, some xylose units are acetylated, which disrupts the intra- and inter-chain hydrogen bonding within the xylan macromolecules (Li et al., 2023; Qaseem & Wu, 2020). This association complicates the preparation of ordered xylan nanocrystals. Nevertheless, crystalline xylan is often found in the dissolving pulp of hemicellulose extracted with concentrated alkaline solutions in industrial viscose fiber mills (Hao et al., 2021). These xylans have a linear structure, as the concentrated alkaline extraction process removes nearly all ferulic acid and acetyl groups, with the primarily consists of xylose and a small amount of arabinose which allows for the formation of both hydrous and anhydrous crystals (Marchessault et al., 1961; Rennie & Scheller, 2014; Yilmaz-Turan et al., 2020). Unlike the nanocrystals of cellulose, chitin, and starch obtained through a top-down strategy that involves removing amorphous regions via methods such as acid hydrolysis, oxidation, or mechanical processes (Seidi et al., 2022), hemicellulose nanocrystals are typically produced using a bottom-up approach, facilitated by solvents such as DMSO or water to promote crystallization. Recently, a variety of physical and chemical methods have been assessed for the preparation of xylan-based nanoparticles and nanocrystals, transitioning from irregular precipitation to stable, regular suspensions. For instance, Meng et al. described a method using dimethyl sulfoxide as a solvent to produce xylan nanocrystals characterized by elongated fibril structures, achieved through a process of crystallization-induced heating lasting 5 to 10 days (Meng et al., 2021). The resulting particle structure exhibited a two-fold crystallization pattern, which differed from earlier studies on xylan hydrate crystals. Wang et al. successfully produced fine xylan nanoparticles with uniform sizes using mild ultrasonication (Wang & Xiang, 2021). Zhang et al. obtained xylan nanoparticles with diameters ranging from 400 nm to 2.5 μm by recrystallizing them under controlled cooling following exposure to elevated temperature and pressure (Zhang, Johnson, et al., 2023). Zhang et al. utilized the evaporation-induced self-assembly (EISA) method to transform nanocluster hydrocolloids into submicron spheroids of nanoxylan. This work established a proof-of-concept for converting amorphous xylan into hierarchical assemblies of crystalline nanoxylan (CNX) as nanomaterials on multiple scales (Zhang et al., 2024). These research findings provide methods for forming size-controlled xylan-based nanoparticles. However, there is still a lack of research on how the structure of xylan itself, especially the presence of branches, affects the morphology and functionality of the nanocrystals/nanoparticles.

The size and morphology of hemicellulose nanoparticles significantly impact various macroscopic properties. Compared with platelet-like nanoparticles, rod-like nanocrystals have a higher aspect ratio, and thus a higher elastic modulus and a more compact aggregation morphology (Han et al., 2020; Torlopov et al., 2017). In addition, the branching of hemicellulose can also affect the morphology and stack structure of its source nanocrystal units. The crystal structure of galactomannan is influenced by the molar ratio of mannose to galactose. As the degree of substitution of galactose increases, the diameter of the unit crystal also increases, while its length remains constant (Song, 1989). Similar results were found in xyloglucan-based nanoparticles, where a lower ratio of galactose side chains turned out to be more slender nanoparticle units that tended to bind and stack closely in parallel, thereby forming large ribbon-like aggregates (Han et al., 2020). The crystal structure of the xylan nanocrystals could be controlled by the degree of substitution, the crystal structure was maintained at low degree of substitution, but was destroyed at high degree of substitution (Lv et al., 2023; Rao et al., 2023; Wang & Xiang, 2021). To address the issue of decreasing crystallinity, researchers have concentrated on developing new technologies for the preparation of hemicellulose nanocrystals. However, the resulting hemicellulose nanoparticles tend to exhibit platelet-like shapes, which diminishes the distinctive advantages associated with nanocrystal units, particularly in terms of chiral self-assembly.

Self-assembly of nanomaterials to create spatially ordered structures presents exciting new opportunities for their applications in electronic devices, biosensor arrays, and biomedical engineering (Bai et al., 2022; Liu et al., 2024; Zhu et al., 2020). Researchers have successfully developed a series of nanocrystal-based functional materials with novel applications, leveraging the self-assembly characteristics of nanocrystals derived from cellulose, starch, and chitin (Li et al., 2024; Liu et al., 2021; Peng et al., 2024). The anisotropic morphology and abundant surface charges of cellulose nanocrystals (CNCs) confer unique assembly behaviors, the most notable of which is their ability to self-assemble into cholesteric liquid crystals exhibiting left-handed chirality in concentrated solutions (Liu et al., 2024). Theoretically, xylan nanocrystals also exhibit left-handed chirality and can self-assemble into specific patterns displaying birefringence through suitable methods. However, research in this area remains limited. One possible reason is that the xylan-based nanoparticles currently obtained are in a platelet shape rather than a rod shape, which may adversely affect their self-assembly behavior. Additionally, the lack of suitable conditions for inducing self-assembly may further hinder progress in this field. By employing confined evaporation-induced self-assembly (C-EISA) with a two-plate system, Wu et al. successfully modified the self-assembly behavior and mechanisms within constrained geometries, resulting in the formation of novel labyrinthine patterns exhibiting birefringence using cellulose nanocrystals that had been modified with side chains (Wu et al., 2024). This may establish new avenues for researching the self-assembly of hemicellulose nanocrystals with side chain modifications.

Sorghum (*Sorghum bicolor (L.) Moench*) is an important crop that holds significant value in food, feed, and energy production due to its high biomass, rapid growth, high sugar content, and strong environmental adaptability (Cheng et al., 2020; Stamenković et al., 2020; Zhang et al., 2023). The lignocellulosic biomass obtained from sorghum can be produced in greater quantities per unit area and time by certain varieties compared to trees, making it a promising source for solid fuels such as bio-pellets and advanced materials, as well as lignocellulosic-derived chemicals. The abundant xylan in sorghum biomass provides a wide range of application potential. However, the research and utilization of sorghum xylan have been somewhat restricted due to a lack of systematic studies and structure-dependent bioproduct preparation schemes.

In this study, we conducted a comprehensive analysis of the structural composition of hemicellulose from 18 natural sorghum accessions, selecting two representative materials: S13, which has a high degree of arabinose branching, and S2, which has a moderate degree of branching. Xylan nanocrystals were prepared using a method involving high-concentration alkaline extraction, ethanol precipitation, and ultrasonic homogenization. The self-assembly of these nanocrystals was further enhanced through confined evaporation-induced self-assembly (C-EISA) using a two-plate system, resulting in the formation of regular patterns exhibiting birefringent characteristics. Compared to S2, the nanocrystals derived from S13 exhibited larger diameters and greater aggregation angles, ultimately leading to more complex macroscopic self-assembly patterns. This study provides new insights into the self-assembly behavior of hemicellulose nanocrystals and lays the foundation for research on low-cost, high-value biomass applications.

2. Materials and methods

2.1. Materials

18 natural sorghum accessions (*Sorghum bicolor*) were collected from the cultivation experimental field of the Shanxi Hou Ji Laboratory in Shanxi Province. The stems of the sorghum were harvested, dried at 60 °C for 48 h, and then ground into a fine powder, which was subsequently sifted through 40-mesh sieves.

Chemical reagents, including potassium hydroxide, ethanol, sodium

chlorite, trifluoroacetic acid, and dimethyl sulfoxide were purchased from Sigma-Aldrich. All chemicals were used as received without further purification.

2.2. Methods

2.2.1. Wall polymers extraction and assay

The extraction and fractionation of cell wall components were carried out following the methods outlined by Peng et al. (2000). Initially, the biomass powders were thoroughly mixed and ground with potassium phosphate buffer (pH 7.0). This was followed by a sequential extraction process involving chloroform-methanol (1:1, *v*/v), DMSO-water (9:1, v/v), and 0.5 % (*v*/v) ammonium oxalate to eliminate lipids, starch, and pectin. The remaining residue was then treated with 4 M KOH containing 1.0 mg/mL sodium borohydride to extract KOH-soluble hemicelluloses. Subsequently, H_2SO_4 (67 %, *v*/v) was applied to completely dissolve cellulose and non-KOH-soluble hemicelluloses. The cellulose content was determined by measuring the hexoses in the cellulose fraction using the anthrone/H_2SO_4 method (Fry, 2000). Total hemicelluloses were quantified by assessing both hexoses and pentoses through the orcinol/HCl method (Dische et al., 1962). The lignin content was analyzed utilizing an assay kit (Solarbio Lot. BC4205). All experimental analyses were performed in biological triplicate to ensure accuracy and reproducibility.

The KOH-extractable and non-KOH-extractable fractions, as described above, were treated with trifluoroacetic acid (TFA) at 120 °C for 1 h after adjusting the pH to neutral. The monosaccharide composition of both KOH-extractable and non-KOH-extractable hemicellulose was analyzed using a high-performance anion-exchange chromatography (HPAEC) system (ICS-5000+, Dionex, USA), which featured a pulsed amperometric detector. Chromatographic separations were executed on a Carbopac PA-20 ion exchange column (3 × 150 mm).

2.2.2. Preparation of xylan

Holocellulose was prepared by initial lignin removal by sodium chlorite (Zhang, Hu, et al., 2023). The dry biomass powders were treated with 8 % (*w*/*v*) sodium chlorite ($NaClO_2$ dissolved in 1.5 % v/v acetic acid) for initial lignin removal under dark at room temperature with 2 cycles (24 h per cycle). For each cycle of treatment, the samples were washed with ultrahigh purity water until pH 7. The remaining biomass residues, termed as holocellulose samples, were washed twice with pure methanol, twice with anhydrous acetone, dehydrated in the hood overnight, and dried in the oven at 50 °C for 2 h. The dried holocellulose samples were ground through a 40-mesh screen and stored in a dry container until use.

The xylan of S2 and S13 were respectively obtained by 4 M KOH extraction with the holocellulose residues. The 4 M KOH fraction was adjusted to pH 5.5–6.6 with acetic acid, and precipitated with 75 % (*v*/v) ethanol. The xylan pellets were collected by centrifugation, washed with 70 % (v/v) ethanol, and freeze-dried until use.

2.2.3. Preparation of xylan nanoparticles

The xylan pellets (obtained as described in section 2.2.2) were dispersed into deionized water with assistance of 40 min ultrasonication at 4 °C, 20 kHz, 320 W then left to stand at least 48 h. Sample S2 and S13 represent xylan nanocrystals prepared at about 4 % (*w*/w).

2.2.4. Self-assembly of xylan nanoparticels in two-plates confined geometry

Glass slides (dimensions: 22 × 40 × 0.15 mm) were first rinsed with deionized water followed by ethanol, and then dried in an oven at 55 °C. Next, 10 μL of a xylan nanoparticle suspension was added dropwise to one side of a glass slide, and a second slide was positioned on top to spread the suspension between the two. The area where the slides overlapped measured approximately 22 × 30 mm. The assembled slides were then left at room temperature (around 25 °C) for 24 h to allow for complete evaporation of the water.

2.3. Characterizations

2.3.1. Immunolabeling

The second internode from S2 and S13 plants at the heading stage was sectioned into 40-μm slices using a paraffin slicer (RM2265, Leica). The sections were analyzed with xylan-specific antibody LM10 and Ara-sidechain-specific antibody CCRC-M154 to visualize the substitution pattern of xylan. Briefly, the sections were incubated with a 5-fold diluted primary antibody for 1.5 h at room temperature, as previously described by Li et al. (2018). Following this, the sections were incubated with a 200-fold diluted secondary antibody (Alexa Fluor 488 anti-mouse IgG, Invitrogen, A1101), which is conjugated to fluorescein isothiocyanate (FITC), in PBS for 1.5 h in darkness. For cellulose staining, the sections were treated with 0.005 % Pontamine Fast Scarlet 4B (S4B) (Sigma, UK) for 15 min in darkness and then washed three times with PBS at room temperature.

2.3.2. 2 D NMR HSQC spectroscopy

All NMR spectroscopy measurements were performed using a Bruker AV600 spectrometer (Bruker, Germany). For sample preparation, either 50 mg of alkaline-extracted hemicellulose was dissolved in 500 μL of deuterium oxide (D_2O) with a few drops of NaOD added, and the mixture was subsequently placed in NMR tubes (Feng et al., 2025). The Heteronuclear Single Quantum Coherence (HSQC) spectrum was recorded in the HSQCGE experimental mode after conducting 64 scans. Data analysis was carried out using MestReNova software.

2.3.3. GPC analysis

The molar mass of the extracted xylan from S2 and S13 was determined using gel permeation chromatography (GPC) with an Agilent 1100 system, which was equipped with multi-angle light scattering (MALS) and differential refractive index (dRI) detectors (Wyatt Technology, United States) (Zhang, Johnson, et al., 2023). For the analysis, 10 mg of xylan was dissolved in 1 mL of a DMSO/LiBr (*v*/v = 95 %: 5 %) solution and subsequently filtered through 0.45 μm filters. DMSO served as the eluent at a flow rate of 0.5 mL/min. A 100 μL aliquot of the xylan solution (5 mg/mL) was injected into the Agilent 1100 system, which included a pump, an autosampler, and a series of columns held at a temperature of 35 °C. The absolute molecular weight was calculated using data obtained from the multi-angle light scattering detector.

2.3.4. X-ray characterization

The X-ray diffraction (XRD) patterns were acquired using a Bruker D8-Advance X-ray diffractometer (Bruker Corp, United States) configured in Bragg-Brentano parafocusing geometry. Xylan nanocrystals were positioned in a glass holder and subjected to scanning under plateau conditions. The X-ray radiation was produced at 40 kV and 18 mA, and the scanning was conducted at a rate of 0.0197°/s, covering a range from 10° to 80°, following the previously established protocol (Hu, Li, et al., 2023).

2.3.5. AFM analysis

The xylan micro/nanoparticle suspension was adjusted to a concentration of 0.1 wt%. A 100 μl aliquot of this suspension was then deposited onto freshly cleaved mica following 30 min of ultrasonic treatment at room temperature. Atomic force microscopy (AFM) imaging was conducted using a Pointprobe™ NCHR-20 probe (NanoWorld, Switzerland), featuring a spring constant of 45 N/m and a tip radius of 8 nm, with a scanning area of 2 μm × 2 μm. The mean thickness of the xylan micro/nanoparticles was determined from the AFM images through the use of NanoScope image analysis software (version 1.90). A minimum of 25 xylan micro/nanoparticles were measured to calculate the average thickness. Furthermore, Image J version 1.45 was used to assess the diameter of the xylan micro/nanoparticles, and the aspect ratio was derived from the measurements of thickness and diameter obtained from the AFM images.

2.3.6. SEM and TEM analysis

The xylan micro/nanoparticles were examined by scanning electron microscopy (ZEISS Sigma 360, Germany). Xylan nanoparticle suspension was added dropwise to a thin glass slide, and a second slide was placed on top to spread the suspension between the two. The assembled slides were then left at room temperature (around 25 °C) for 24 h to allow for complete evaporation of the water. After removing the top glass slide, the individual nanoparticles, the macroparticles form by aggregation of nanoparticles, and the self-assembly wall were observed using scanning electron microscopy. The crystal diffraction of xylan nanoparticle was observed using transmission electron microscopy (TEM, JEOL JEM-F200, Japan), as described in a previous study (Amin et al., 2013).

3. Results and discussion

3.1. Comprehensive analysis of hemicellulose in sorghum straw

The analysis of the main components of the cell wall in powdered straw from 18 representative sorghum materials showed that the cellulose levels were varied from 22.30 % to 36.43 % (% dry matter), the hemicellulose content ranged from 18.50 % to 32.53 %, and the lignin content ranged from 10.08 % to 17.05 % (Fig. 1A, Table S1). Analysis of the hemicellulose monosaccharides in the 18 types of sorghum biomass materials showed that xylose (Xyl) and arabinose (Ara) were the predominant monosaccharides in the alkali-soluble (KOH-extractable) hemicellulose (Fig. 1B). In contrast, Xyl, glucose (Glc), and Ara were the primary monosaccharides in the alkali-insoluble (non-KOH-extractable) hemicellulose (Fig. 1C). We further calculated the molar ratio of arabinose to xylose (Ara/Xyl), which serves as an indicator of the branching ratio of arabinoxylan. The Ara/Xyl ratios in the KOH-extractable hemicellulose ranged from 0.06 to 0.20, with a coefficient of variation (*C.V.*) of 29.14. In contrast, the ratios in the non-KOH-extractable hemicellulose ranged from 0.14 to 0.22, with a *C.V.* of 11.01 (Fig. 1D, Table S1).

Sorghum possesses advantages such as high biomass and rapid growth, and it has a higher hemicellulose content compared to other species, making it an important raw material for hemicellulose in both food and industrial applications (Wang et al., 2021). Our findings indicate that xylan is the predominant component of hemicellulose in 18 sorghum varieties, exhibiting substantial variation in both content and branching degree (Fig. 1). Furthermore, it was found that the alkali-insoluble hemicellulose contains xylan with a higher degree of branching (Fig. 1D), which is consistent with reports from other species and suggests that it is closely cross-linked with cellulose (Gao et al., 2020; Wang et al., 2016).

The structural diversity and heterogeneity of AX lead to significant differences in its biological properties. Current research on xylan branching and its biological characteristics focuses on processing conditions and separation methods, using debranching enzymes or various chemical treatments to obtain xylans with different substitution structures. However, these methods increase processing complexity and costs. In our study, we identified a representative material, S13, which exhibits a significantly higher Ara/Xyl ratio compared to the other materials and showed consistent results in both alkali-soluble and alkali-insoluble hemicellulose (Fig. 1D). This characteristic not only facilitates the acquisition of xylan raw materials with notable structural differences under minimal processing conditions, but also help to reduces the errors introduced by the processing methods.

3.2. Structural characterization of xylan from S2 and S13 straw

Based on the comprehensive analysis above, we selected S13 along with another representative material, S2, which has an Ara/Xyl ratio closer to the average level, for further investigation. To understand the distribution of xylan in S2 and S13, we used the xylan-backbone-specific LM10 antibody and CCRC-M154, which specifically targets the arabinose sidechains of xylan, to visualize xylan in the stem sections of both materials (Fig. 2A). A relatively weak LM10 signal was observed in the S13 section compared to S2 (Fig. 2A&B). Furthermore, the intensity of the CCRC-M154 signal in S13 was significantly stronger than in S2 (Fig. 2A & C). To gain a deeper understanding of the xylan substituted pattern in the straw of S2 and S13, we employed High-Performance Anion-Exchange Chromatography (HPAEC) to analyze the monosaccharide composition. The results indicated an increase in the peak area for Ara and a decrease in the peak for Xyl (Fig. 2D-F) in S13. Specifically, the ratio of the peak area of Ara to Xyl was calculated to be 0.09 for S2 and 0.20 for S13 (Fig. 2G). These findings provide clear evidence that S13 contains a higher amount of arabinose, with approximately one arabinose sidechain modification for every 5 to 6 xylose residues. Furthermore, the weak signals for glucuronic acid (GlcA) in the HPAEC analysis indicate a predominance of Ara over GlcA sidechains in the KOH-extractable xylan of sorghum straw (Fig. 2D).

NMR is a powerful analytical tool for the resolution of the detailed structure of natural polymers when signal assignments have been assigned from known structures. To better elucidate the xylan structure in the S2 and S13, alkali-extracted hemicellulose from the holocellulose was subjected to 2D HSQC NMR analysis (Fig. 3). The assignment of characteristic peaks to corresponding atoms was carried out according to previously established methods (Feng et al., 2025; Shen et al., 2021). The $^{13}C/^{1}H$ cross peaks at δ 101.42/4.36 (Xyl_1), 72.50/3.18 (Xyl_2), 73.38/3.44 (Xyl_3), 76.14/3.67 (Xyl_4), 62.65/3.26 ($Xyl_{5\text{-}ax}$), and 62.64/3.99 ($Xyl_{5\text{-}eq}$) are assigned to (1 → 4)-β-d-Xyl*p*, which forms the xylan backbone. The signals for the α-L-Ara*f* are clearly identified at the cross

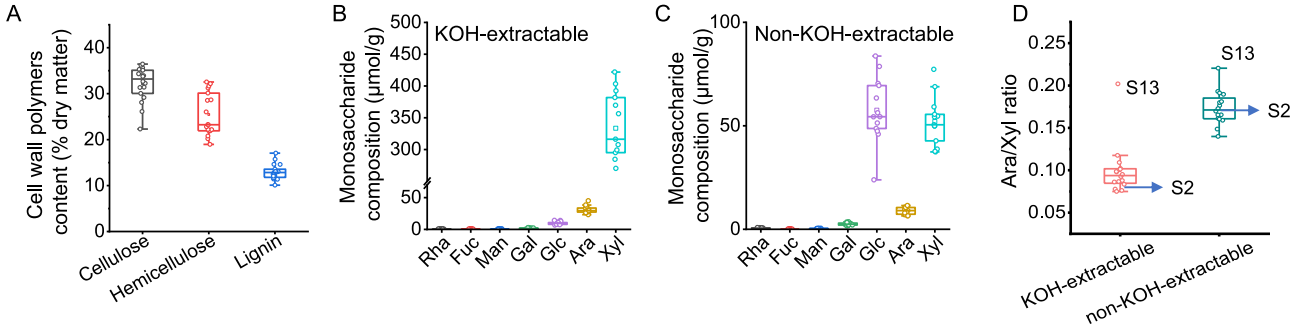

Fig. 1. Comprehensive analysis of hemicellulose in sorghum straw. A, Diversity of cell wall composition among sorghum accessions. B—C, Neutral monosaccharide analysis using GC–MS, Rha representing rhamnose, Fuc for fucose, Man for mannose, Gal for galactose, Glc for glucose, Ara for arabinose, Xyl for xylose, B, monosaccharide composition in the fraction extracted with 4 M KOH, C, monosaccharide composition of residues after treatment with 4 M KOH. D, The ratio of arabinose to xylose. Date points represent the means of three biological replicates of each sorghum samples, and error bars indicate the standard deviation across 18 accessions. $n = 18$.

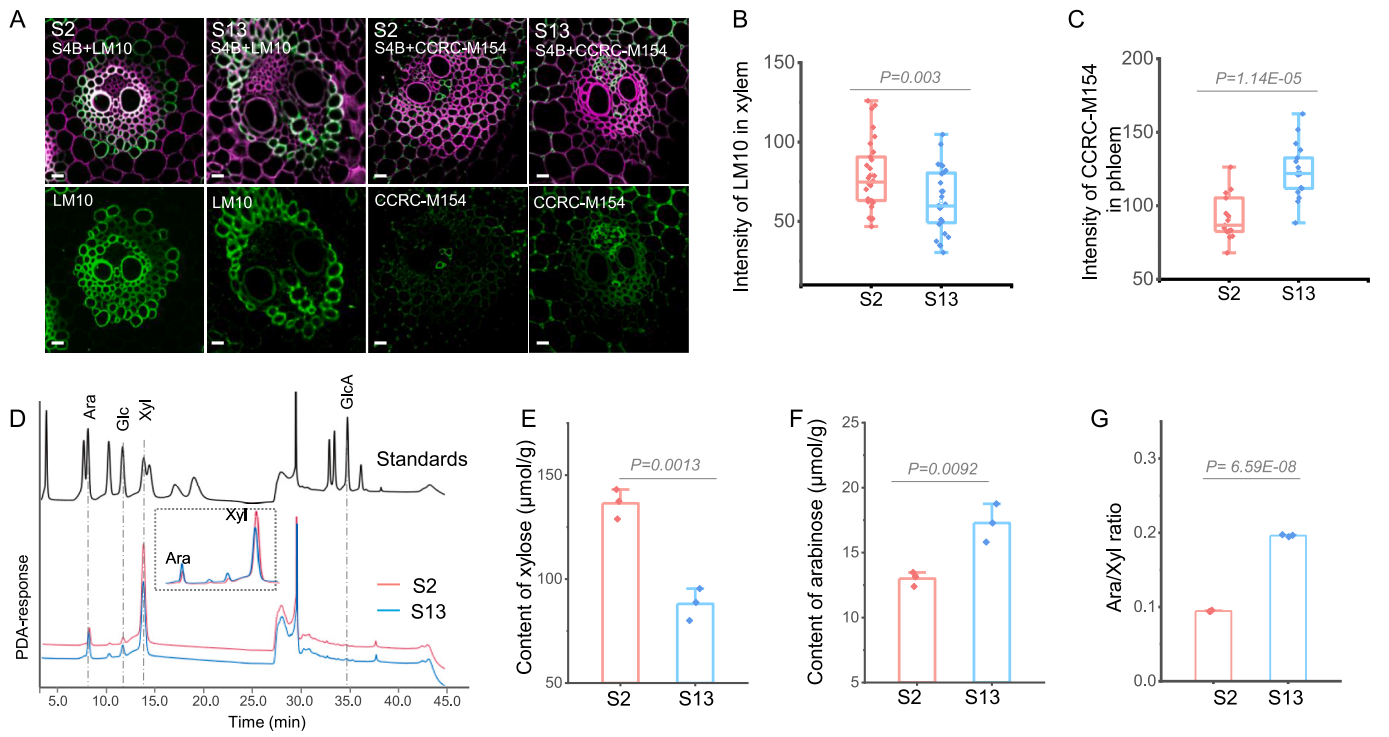

Fig. 2. Characterization of arabinose substitution pattern on xylan from varieties S2 and S13. A, In situ immunolabeling of arabinoxylan (AX) in the internodes of S2 and S13 during the jointing stage. LM10 and CCRC-M154 are antibodies that target the backbone and arabinose side chains of arabinoxylan (AX), respectively. S4B is the dye used for cellulose staining, Bar = 50 μm in all images. B—C, Fluorescence intensity of the LM10 and CCRC-M154 in xylem as illustrated in A, Data source includes at least 25 fluorescence spots from no fewer than 3 images, *P* value was determined using *Student's t-test*. D-G, Sugar compositional analysis of S2 and S13 by HPAEC-PAD, D, HPAEC-PAD chromatogram of monosaccharides, E, content of Xyl, F, content of Ara, G, arabinose to xylose ratio, data as mean ± SD ($n = 3$), *P* value was determined using *Student's t-test*.

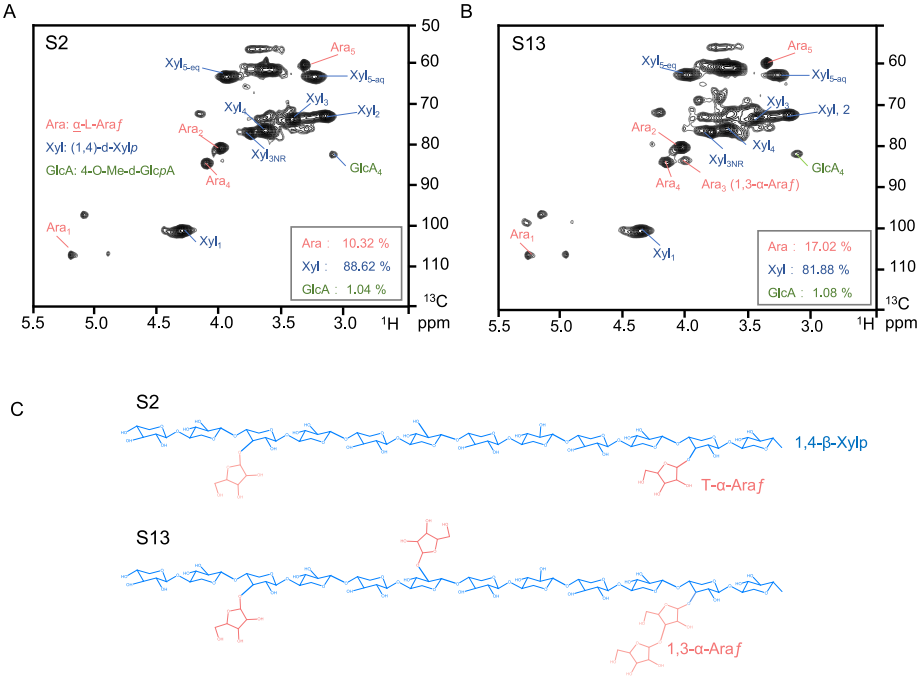

Fig. 3. Xylan structure analysis of S2 and S13 by NMR. A-B, HSQC spectra of hemicellulose fractions extracted from the S2 (A) and S13 (B) straw. Xyl: (1, 4) linked β-d-Xylp; GlcA: 4-*O*-methyl-α-D-glucuronic acids; Ara: α-L-Ara*f*. a = axial, e = equatorial. C. The putative structural schematic diagram of AX from S2 and S13 according to Shen et al. (2021).

peaks of δ 107.51/5.28 (Ara_1), 80.53/4.05 (Ara_2), 84.46/4.16 (Ara_4), 59.63/3.55 (Ara_5). Interestingly, a distinct signal for Ara_3 with 1,3-α-Araf (83.32/3.98) is clearly identified at S13, while it is only weakly present in S2. It is speculated that the xylan in S13 contains secondary arabinose modifications (Fig. 3C) (Shen et al., 2021). In addition, the NMR 2D HSQC analysis revealed a corresponding cross peak at 82.21/3.12 (GlcA4), which is associated with glucuronic acid. The relative content results obtained from peak area calculations indicate that the glucuronic acid content is relatively low, approximately 1 %, with no significant differences observed between samples S2 and S3 (Fig. 3A & B). This finding aligns with the results obtained from the HPAEC method for measuring acidic sugars mentioned earlier, suggesting that glucuronic acid is not a major factor influencing the structure of xylan extracted from S2 and S13 under high-concentration alkaline conditions.

The molecular weight of xylan is crucial for evaluating its performance in various applications. To gain a deeper understanding of the industrial properties, we measured the molecular weight of KOH-extractable xylan derived from the holocellulose of S2 and S13 using Gel Permeation Chromatography (GPC) (Fig. 4; Table 1). Both S2 and S13 exhibited similar weight-average molecular weights (Mw) of 90.4 kDa; however, they differed in their number-average molecular weights (Mn), with values of 59.9 kDa for S2 and 66.8 kDa for S13 (Table 1). The identical Mw combined with a higher Mn indicates, to some extent, that the sample possesses a broader molecular weight distribution or features more complex side chain modifications. Considering the elution time and molecular weight distribution results (Fig. 4), it indicates that the xylan derived from S13 has a similar molecular weight distribution size to that from S2, but features more complex side chain modifications.

3.3. *Ara side-chain regulates the morphology of xylan nanoparticles*

Xylan-derived nanoparticles are innovative materials that leverage the unique properties of xylan. Due to their natural origin, xylan-derived nanoparticles are non-toxic and environmentally friendly, making them suitable for a wide range of applications. The xylan nanoparticles derived from alkali-extracted hemicellulose of S2 and S13 were obtained by resuspending the hemicellulose in ultrapure water, treating it with ultrasound for 40 min, and allowing it to sit at least 48 h at 4 °C (Fig. S1A). The resulting homogeneous xylan nanoparticles remained uniform during long-term storage (over 3 months), demonstrating their excellent aqueous dispersibility (Fig. S1B). Given that the characterization of nanoparticles is vital for a thorough understanding of the origins of their behavior, we performed comprehensive imaging of the nanoparticles derived from S2 and S13 samples using AFM (Fig. 5A), SEM (Fig. 5B), and TEM (Fig. 5C). To improve the comparability of the nanoparticle properties, the size and shape, which are the most prominent physicochemical properties of nanoparticles, were accurately characterized, as shown in Fig. 5 D—F. For each sample, at least three

Table 1
Molecular weight of the hemicellulose extracted by alkaline from S2 and S13.

	Mn	Mw	Mw/Mn
S2	59,926	90,429	1.5
S13	66,824	90,439	1.3

replicates were carried out to ensure reproducibility. The nanoparticles with a minimum size interval were considered as the smallest measurable individuals and were thus identified as primary aggregates (Han et al., 2020; Hirschle et al., 2016). The detailed measurement methods for the nanoparticles are shown in Fig. S2, where a, b, and c represent the height, width, and length of the nanocrystal unit, respectively. According to the observed image and collected data, the nanoparticles were elliptical in shape, which is different from the elongated rod-like structures formed in DMSO solvent and the disc-like structures formed at high temperatures (Meng et al., 2021; Zhang, Johnson, et al., 2023). These characteristics of elliptic shape and flatness of xylan nanoparticles were found to be quite in accordance with XNC obtained under ultrasonic colloidal dispersion (Wang & Xiang, 2021), however, there are significant differences in the morphology of nanoparticles prepared from xylan with distinct branching features. Specifically, as depicted in the AFM images, the nanoparticles from S13 were rounder compared to those from S2 (Fig. 5A). Although the primary aggregates of nanoparticles from S13 did not show significant differences in length (Fig. 5D, Fig. S3), their height and width were notably bigger than those of the nanoparticles from S2 (Fig. 5E & F, Fig. S3). This is consistent with the observations made from the SEM scans, although most nanoparticles sourced from S2 are oriented vertically, it is also evident that the particles from S13 are generally larger (Fig. 5B). Furthermore, this finding aligns with the size distribution analysis conducted via dynamic light scattering (DLS), which revealed that the nanoparticles derived from S13 are larger than those from S2 (Fig. 5G). Another notable change observed was the higher length-to-width ratio (c/b) in S2 (1.42 ± 0.16) compared to S13 (1.22 ± 0.01), indicating that these primary aggregates have a more slender morphology (Fig. 5A). Interestingly, in this study, although it is challenging to identify individual nanoparticles using TEM, these particles exhibit typical characteristics of crystal diffraction (Fig. 5C). As previous studies have shown that the crystalline properties of hemicellulose nanoparticles are closely associated with their degree of branching (Rao et al., 2023), an X-ray diffraction (XRD) study was conducted to further investigate this phenomenon, with the results presented in Fig. 5H. The xylan nanoparticles exhibited a typical xylan hydrate crystal characteristic, with a peak intensity observed at a *2-Theta* value of 19.9° (200) (Zhang et al., 2024). In comparison to the S13 samples, S2 displayed a higher intensity of the diffraction peak (Fig. 5H), suggesting that the nanoparticles derived S2 have a higher degree of crystallinity (*CrI*). This indicates that xylan with lower arabinose content possesses more ordered structures and higher *CrI*.

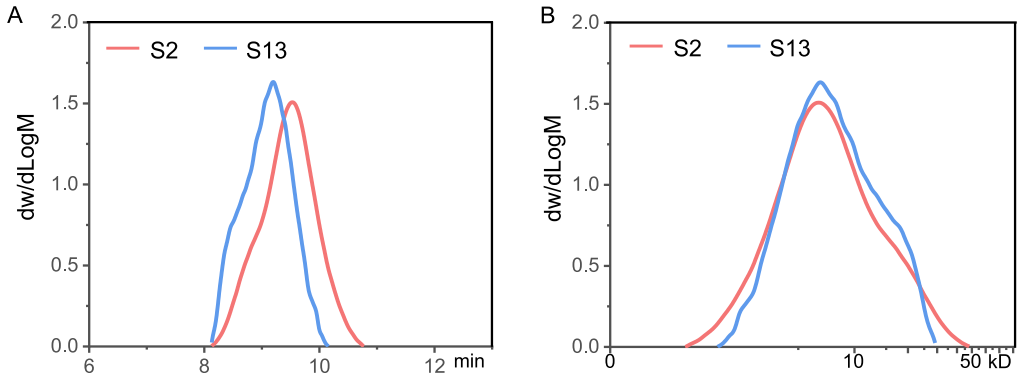

Fig. 4. GPC trace of extracted xylan. A, The elution time. B, The molecular weight distribution.

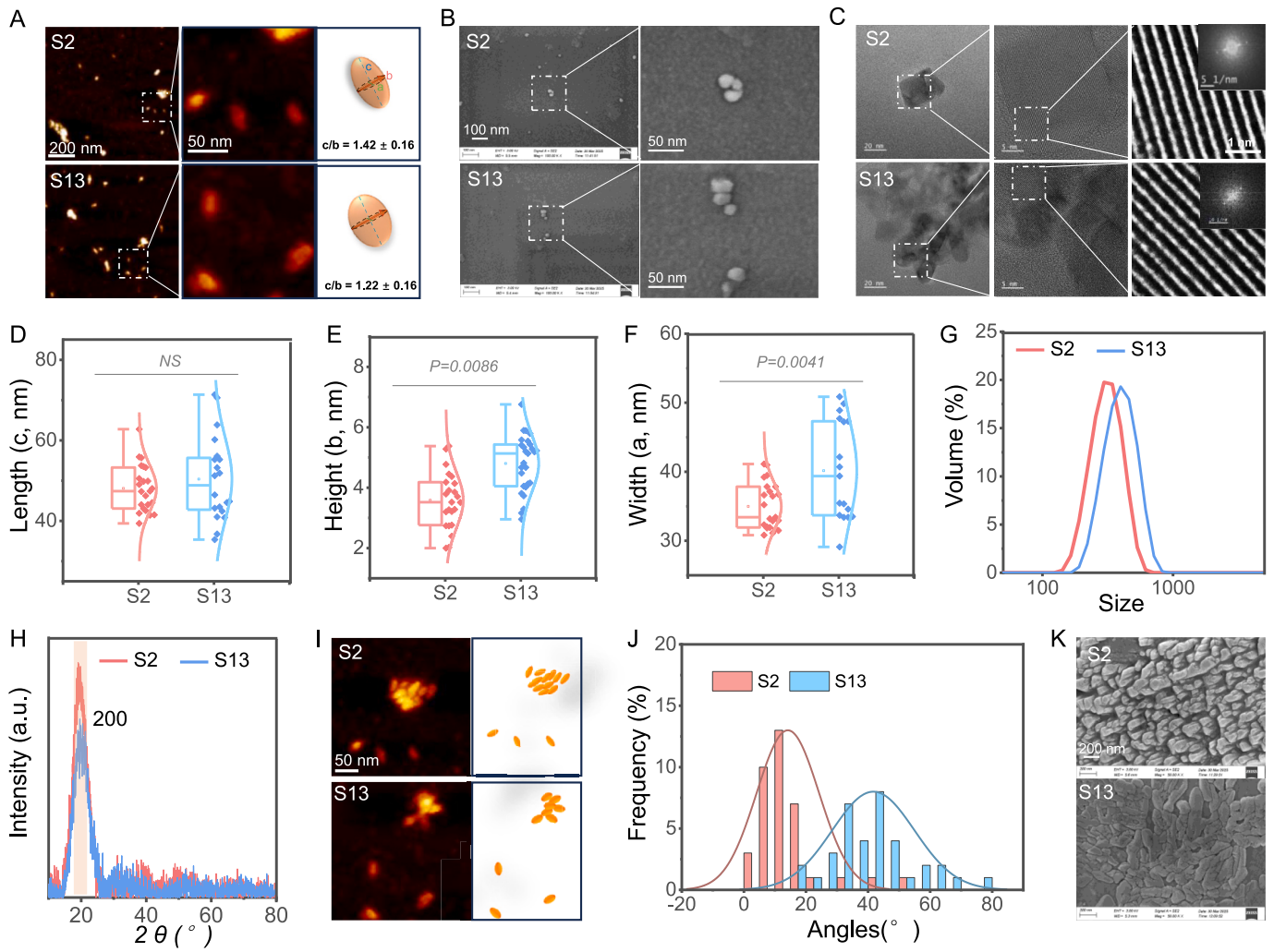

Fig. 5. Characterization of the morphology of xylan nanoparticles. A. AFM height images of xylan nanoparticles, scale bar = 200 nm, 50 nm. B. SEM images, scale bar = 100 nm, 50 nm. C. TEM image and diffraction analysis, scale bar = 20 nm, 5 nm, 1 nm. D—F, Measurement of nanoparticles morphology, D, length, E, height, F, width. Data source includes at least 30 nanoparticles from no fewer than 3 images, data points and bars refer to mean values and standard deviation, respectively. *P* value was determined using *Student's t-test*. G, DLS curves. H, XRD curves. I-J, AFM observation of self-assembly behavior of xylan nanoparticles. I, AFM height images of multiple primary aggregates, scale bar = 50 nm, J, measurement of nanoparticle arrangement angles. K. SEM images of multiple primary aggregates, scale bar = 200 nm.

Additionally, it was observed that the larger-sized macroparticles had well-defined shapes, and these macroparticles were inferred to be aggregates composed of multiple primary aggregates (Fig. 5I & K). Representative evidence of binding is presented in Fig. 5I and K, which were imaged using AFM and SEM, respectively. This suggests that these macroparticles may have originated from the initial binding of two or more individuals, followed by fusion. The nanoparticles in S2 exhibited a strong tendency to bind with other particles in near-parallel orientations, while those from S13 displayed different characteristics, showing irregular and loosely aggregated arrangements at larger angles (Fig. 5I -J & K, Fig. S4 A & B). This behavior has not been reported in the aggregation state of xylan nanoparticles but is similar to that observed in nanoparticles derived from another type of hemicellulose, galactose modified xyloglucan (Han et al., 2020).

Looking back to the above results, the long-term stability and uniformity of xylan nanoparticles during storage indicate their excellent aqueous dispersibility, which is crucial for their applications in aqueous systems. The differences in shape and size between nanoparticles derived from S2 and S13, particularly the rounder particles from S13, suggest that the branching features of the xylan source significantly impact particle morphology, a finding further supported by dynamic light scattering (DLS) and X-ray diffraction (XRD) results. Compared to S13, the nanoparticles from S2 are more prone to compact parallel aggregation when forming macroparticles, leading to the tendency to create planar layered structural patterns. The varying abundance of arabinose residues can influence self-assembly patterns and properties by modulating the morphology of the primary particles. Understanding these relationships can optimize the production processes of nanoparticles to achieve desired characteristics for specific applications, ultimately contributing to the development of sustainable materials based on renewable resources.

3.4. *Effect of Ara side-chain on the self-assembly behavior of xylan nanoparticles*

The self-assembly behavior of nanoparticles involves the autonomous formation of ordered structures through non-covalent interactions, including hydrogen bonding, electrostatic forces, and hydrophobic interactions (Liu et al., 2024; Seidi et al., 2022). The structures generated through self-assembly not only possess functional potential for applications such as drug delivery, environmental remediation, and biosensor development but also enhance the mechanical

properties and biocompatibility of materials (Bai et al., 2022). Moreover, the birefringent response of elastic materials with rich polarized interference colors shows great promise in the field of stretchable optics. The chiral self-assembly and birefringent properties of linear polysaccharides such as cellulose and chitin nanocrystals obtained through top-down approaches have been widely studied in various fields (Huang & Wei, 2012). In contrast, although hemicellulose-derived nanoparticles exhibit certain crystalline characteristics, the heterogeneity in their morphology and size, along with the restricted preparation conditions, has limited the exploration of their chiral self-assembly and birefringent properties. In recent years, confined evaporation-induced self-assembly (C-EISA) has emerged as an efficient method and has been widely used to study the self-assembly of various nanoparticles because it can provide real-time insights into the self-assembly process under controlled evaporative conditions (von Baeckmann et al., 2021; Wu et al., 2024). This slow and uniform process is crucial for observing the dynamic behavior of xylan nanocrystals and understanding the structure-function relationship in our study. In this study, we employed the C-EISA technique to investigate the self-assembly process of xylan-derived nanoparticles from S2 and S13.

The C-EISA of xylan nanoparticles occurs in a parallel-plate geometry formed by two glass slides, and the entire process is conducted at room temperature according to Wu et al. (Wu et al., 2024). In comparison to water and 1 % (*w*/w) xylan suspensions, we successfully observed a stable branched structure pattern in the xylan nanoparticle samples at the same concentration (Fig. S5). Using polarized light microscopy, we observed the self-assembled patterns of xylan nanoparticles, which resemble labyrinthine structures but are more intricate (Fig. 6). This behavior may be attributed to the lower colloidal stability of the xylan nanoparticles, contrasting sharply with the regular rainbow-like lamellar patterns observed in cellulose (Wang et al., 2023). Overall, the patterns formed by xylan nanoparticles derived from S2 in a double-

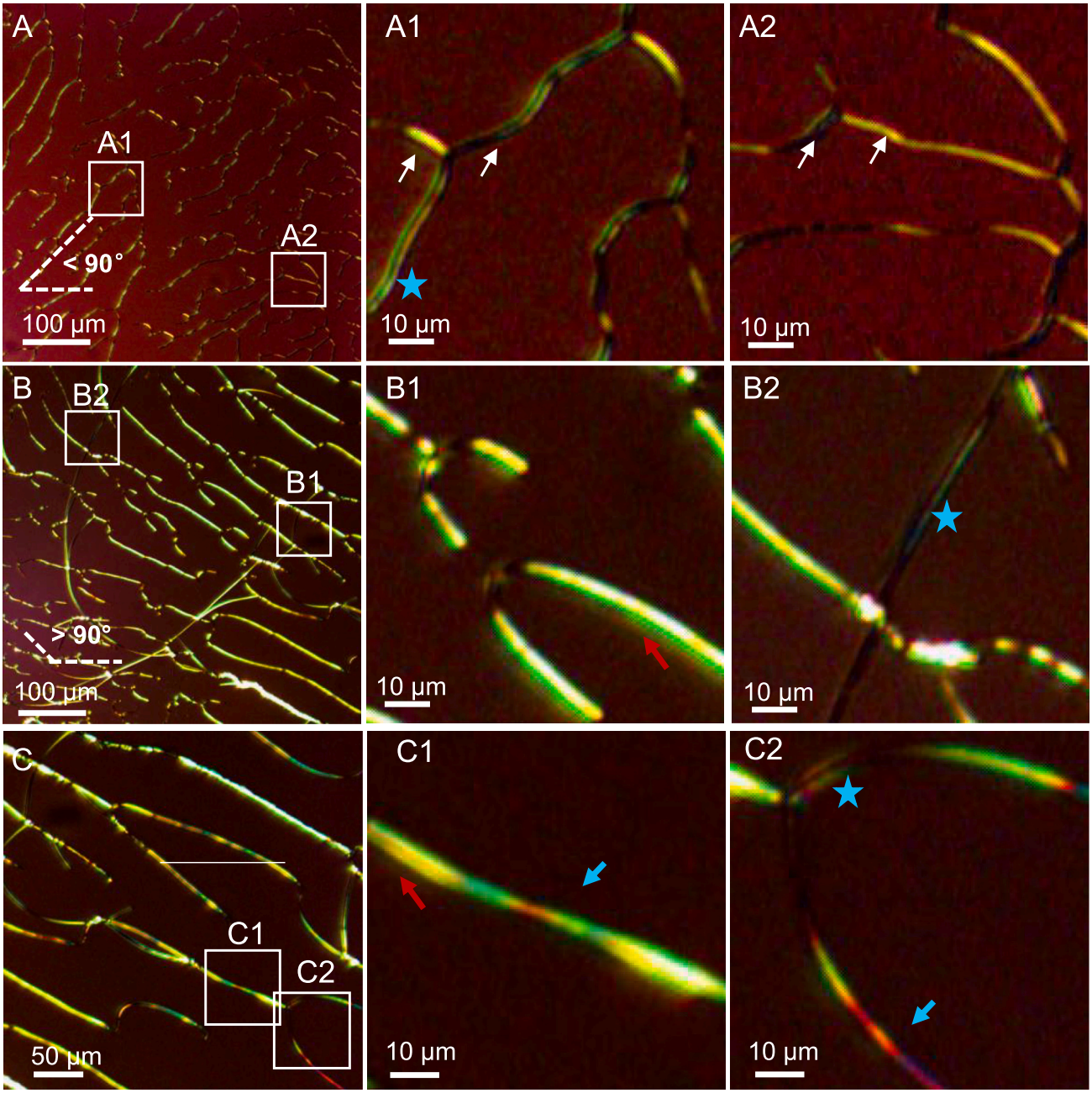

Fig. 6. Varied and intricate self-assembled patterns of xylan nanoparticles observed using polarized optical microscopy (POM), scale bar = 100 μm, 50 μm, 10 μm.

layer glass setup through C-EISA exhibit distinct directionality, which can be broadly categorized into two types: those with angles less than 90° and those greater than 90 degrees (Fig. 6 A & B). It can be observed that the walls exhibit yellow and green colors when their long axial direction is approximately 45° and 135°, respectively (Fig. 6 A1 & A2, white arrow). This pronounced birefringent effect serves as intuitive evidence for the long-range order present in the self-assembly structure. Interestingly, at higher magnifications, the lamellar (Fig. 6 A1, B2 and C2, blue stars), tubular (Fig. 6 B1 & C1, red arrows), and distinct helical (Fig. 6 C1 & C2, blue arrows) structures can be clearly observed, displaying a vivid array of iridescent colors (Fig. 6).

To identify the effect of arabinose side chain on the self-assembly behavior, we strictly controlled the entire experimental process and carefully compared self-assembly patterns at the same position and angle with no less than three repetitions (Fig. 7). Utilizing polarized light microscopy to observe the self-assembly patterns with long-axis directions greater than 90°, we found that the maze - like self-assembled patterns derived from S13 exhibited a richer variety of helical types and iridescent colors compared to those from S2 (Fig. 7 A, white arrow, Fig.S5). Furthermore, scanning electron microscopy was employed to examine the helical locations, branching and long arm positions (Fig. 7 B). The results revealed that, in contrast to the dense and regular structures assembled from S2, the self-assembled walls from S13 displayed irregular particles, consistent with previous observations (Fig. 5 K). We also conducted preliminary measurements and characterizations of the self-assembly patterns of nanoparticles from both sources with at least three repetitions (Fig. 7 C-E). The results demonstrated that S13 exhibited a higher number of branches and shorter arm lengths compared to S2, while the overall branching angles remained statistically similar (Fig. 7 C-E, Fig.S5). The primary structural distinction between the xylans from S2 and S13 is the modification by arabinose side chains, suggesting that the observed differences are predominantly due to these branching structures. The arabinose modification is closely linked to the spatial conformation of xylan molecules. Lower branching degrees tend to facilitate the formation of parallel secondary structures, whereas side-chain modification promotes the development of spatially twisted tertiary structures within xylan molecules (Grantham et al., 2017). Furthermore, side-chain modifications may influence intermolecular forces through steric hindrance during the aggregation of xylan, resulting in a relatively lower crystallinity (Lv et al., 2023; Rao et al., 2023; Wang & Xiang, 2021). Consequently, S13, characterized by its higher branching degree, may face greater challenges in forming consistent nanocrystals. This steric hindrance, along with the interplay of intermolecular forces, further impacts the arrangement and aggregation states of the nanoparticles.

Although hemicellulose-derived nanoparticles exhibit certain crystalline characteristics, their morphological and size heterogeneity, along with limitations in preparation conditions, still restricts the exploration of their chiral self-assembly and birefringent properties. The pronounced birefringent effect we observed provides intuitive evidence for long-range order within the self-assembled structures. This finding not only enriches our understanding of the self-assembly behavior of xylan nanoparticles but also offers new insights for further research on functional materials in the field of hemicellulose. Overall, this study reveals

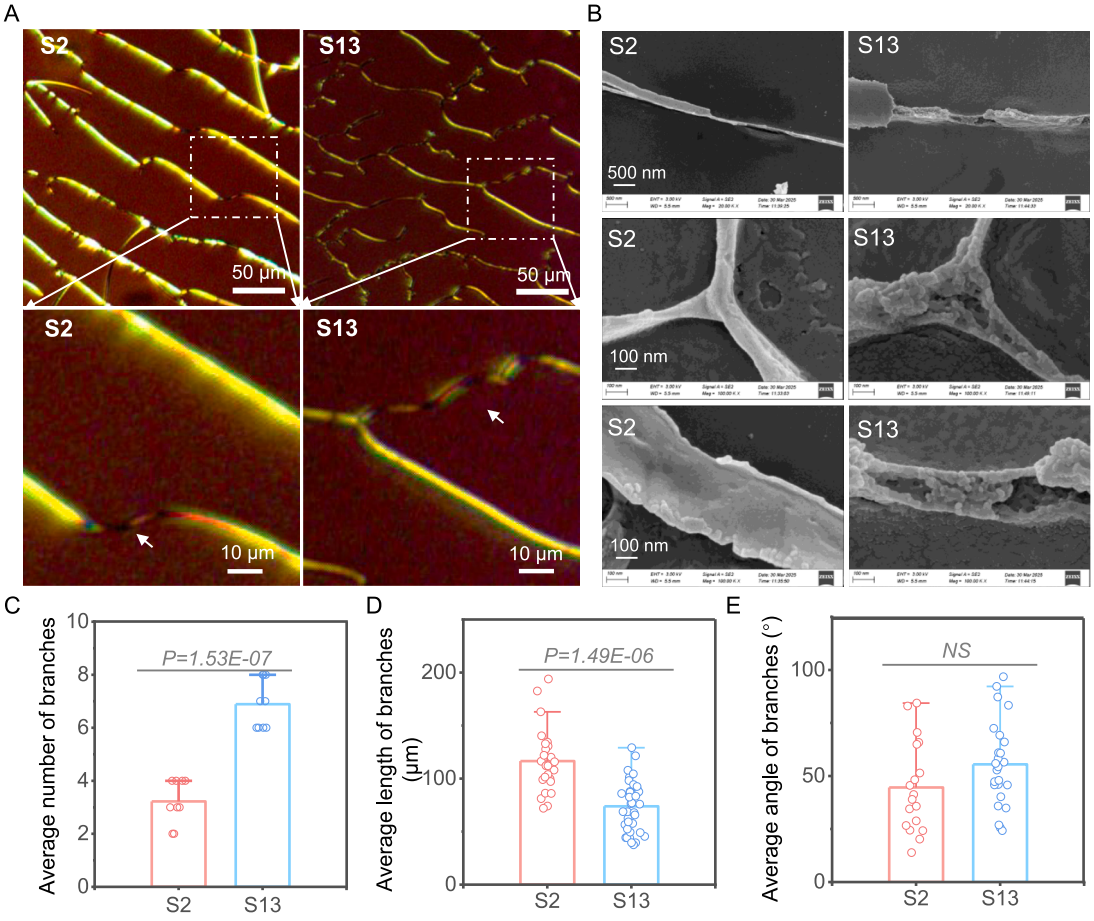

Fig. 7. Investigation of self-assembled patterns in xylan nanoparticles derived from S2 and S13. A. POM images, scale bar = 50 nm, 10 nm. B. SEM images, scale bar = 500 nm, 100 nm. C-E. Quantitative analysis of branching in self-assembled patterns, C, number of branches, D, length of branches, E, angle of branches. The data source includes at least 6 self-assembled walls in panel C and 20 branches in panels D and E, derived from no fewer than 3 images. Data points and error bars refer to mean values and standard deviation, respectively. *P* value was determined using *Student's t-test.*

the influence of the arabinose side chain on the self-assembly characteristics of xylan nanoparticles, highlighting the importance of a deeper understanding of self-assembly mechanisms in the development of functional materials. These findings will lay a new foundation for future research in the field of hemicellulose and its derived materials, potentially advancing the development of novel materials for applications such as drug delivery and biosensors.

4. Conclusions

This study comprehensively analyzed the hemicellulose composition and structural characteristics of xylan derived from different sorghum varieties, specifically S2 and S13. Our findings revealed significant variations in the arabinose to xylose (Ara/Xyl) ratios, indicating differing degrees of branching in the xylan structures. Notably, S13 exhibited a higher Ara/Xyl ratio and a more complex branching structure compared to S2. This difference was reflected in the distinct morphologies of the nanoparticles and self-assembly behaviors observed. The xylan nanoparticles derived from S13 showed rounder shapes, larger sizes, and a greater tendency for irregular aggregation, suggesting that arabinose side chains play a crucial role in modulating their morphology and self-assembly patterns. The robust self-assembly of xylan nanoparticles, driven by non-covalent interactions, suggests their potential for a range of functional applications in biomedicine and environmental technology. Moreover, the pronounced birefringent effects observed in the self-assembled structures of xylan nanoparticles highlight the potential for these materials in advanced applications such as drug delivery and biosensing. Overall, this research provides valuable insights into the structural diversity and functionality of hemicellulose-derived materials, paving the way for future investigations into the optimization and application of xylan nanoparticles in various fields.

CRediT authorship contribution statement

Youmei Wang: Writing – original draft, Investigation, Funding acquisition, Formal analysis. **Yaoyao Zhu:** Validation, Methodology, Conceptualization. **Min Li:** Visualization, Validation, Methodology. **Bingyi Ji:** Methodology. **Shisheng Liu:** Methodology. **Weiqing Liu:** Investigation. **Zhen Hu:** Methodology, Funding acquisition. **Hui Zhang:** Methodology. **Wei Zhang:** Writing – review & editing, Funding acquisition. **Liangcai Peng:** Supervision, Conceptualization. **Zhaosheng Kong:** Writing – review & editing, Supervision, Investigation, Funding acquisition, Conceptualization.

Declaration of competing interest

The authors declare that they have no known competing financial interests or personal relationships that could have appeared to influence the work reported in this paper.

Acknowledgements

This work was in part supported by the National Natural Science Foundation of China (32370286, 32400212, 32241038, 32241041), the National Key Research and Development Program of China (2023YFD1202704), the Distinguished and Excellent Young Scholar Cultivation Project of Shanxi Agricultural University (2023YQPYGC04).

Appendix A. Supplementary data

Supplementary data to this article can be found online at https://doi.org/10.1016/j.carbpol.2025.123874.

Data availability

Data will be made available on request.

References

Amin, M., Iram, F., Iqbal, M. S., Saeed, M. Z., Raza, M., & Alam, S. (2013). Arabinoxylan-mediated synthesis of gold and silver nanoparticles having exceptional high stability. *Carbohydrate Polymers, 92*, 1896–1900. https://doi.org/10.1016/j.carbpol.2012.11.056

Bai, L., Liu, L., Esquivel, M., Tardy, B. L., Huan, S., Niu, X., & Rojas, O. J. (2022). Nanochitin: Chemistry, structure, assembly, and applications. *Chemical Reviews, 122*, 11604–11674. https://doi.org/10.1021/acs.chemrev.2c00125

Cheng, M. H., Kadhum, H. J., Murthy, G. S., Dien, B. S., & Singh, V. (2020). High solids loading biorefinery for the production of cellulosic sugars from bioenergy sorghum. *Bioresource Technology, 318*. https://doi.org/10.1016/j.biortech.2020.124051

Dische, Z., Pallavicini, C., Kavasaki, H., Smirnow, N., Cizek, L. J., & Chien, S. (1962). Influence of the nature of the secretory stimulus on the composition of the carbohydrate moiety of glycoproteins of the submaxillary saliva. *Archives of Biochemistry and Biophysics, 97*, 459–469. https://doi.org/10.1016/0003-9861(62)90108-X

Feng, A., Guan, Y., Yang, H., Zheng, B., Zeng, W., Hao, P., & Wu, A.-m. (2025). Characterization of hemicellulose in sacred lotus (*Nelumbo nucifera* Gaertn.) petiole during xylogenesis. *Carbohydrate Polymers, 349*, Article 122940. https://doi.org/10.1016/j.carbpol.2024.122940

Fry, S. C. (2000). *The growing plant cell wall: Chemical and metabolic analysis*. London, Book: Longman, 1-930665-08-3 http://www.blackburn-press.com/growplancelw.html.

Gao, Y., Lipton, A. S., Wittmer, Y., Murray, D. T., & Mortimer, J. C. (2020). A grass-specific cellulose–xylan interaction dominates in sorghum secondary cell walls. *Nature Communications, 11*, Article 6081. https://doi.org/10.1038/s41467-020-19837-z

Gericke, M., Geitel, K., Jörke, C., Clement, J. H., & Heinze, T. (2021). Reactive nanoparticles derived from polysaccharide phenyl carbonates. *Molecules, 26*. https://doi.org/10.3390/molecules26134026. Article 4026. https://doi.org/.

Grantham, N. J., Wurman-Rodrich, J., Terrett, O. M., Lyczakowski, J. J., Stott, K., Iuga, D., & Dupree, P. (2017). An even pattern of xylan substitution is critical for interaction with cellulose in plant cell walls. *Nature Plants, 3*, 859–865. https://doi.org/10.1038/s41477-017-0030-8

Han, M., Liu, Y., Zhang, F., Sun, D., & Jiang, J. (2020). Effect of galactose side-chain on the self-assembly of xyloglucan macromolecule. *Carbohydrate Polymers, 246*, Article 116577. https://doi.org/10.1016/j.carbpol.2020.116577

Hao, X., Li, N., Wang, H., Jia, S., Liu, Q., & Peng, F. (2021). Dialdehyde xylan-based sustainable, stable, and catalytic liquid metal nano-inks. *Green Chemistry, 23*, 7796. https://doi.org/10.1039/D1GC02696H

Hirschle, P., Preiß, T., Auras, F., Pick, A., Völkner, J., Valdepérez, C., & Wuttke, S. (2016). Exploration of MOF nanoparticle sizes using various physical characterization methods – Is what you measure what you get. *CrystEngComm, 18*. https://doi.org/10.1039/C6CE00198J. Article 4359.

Hu, Z., Li, Q., Chen, Y., Li, T., Wang, Y., Zhang, R., & Peng, L. (2023). Intermittent ultrasound retains cellulases unlock for enhanced cellulosic ethanol with high-porosity biochar for dye adsorption using desirable rice mutant straw. *Bioresource Technology, 369*. https://doi.org/10.1016/j.bio-rtech.2022.128437. Article 128437.

Huang, Y., & Wei, Z. (2012). Self-assembly of chiral amphiphiles with π-conjugated tectons. *Chinese Science Bulletin, 57*, 4246–4256. https://doi.org/10.1007/s11434-012-5470-y

Li, H. Y., Wang, Y. P., Zhao, P., Guo, L. P., Huang, L. Q., Li, X., & Gao, W. Y. (2023). Naturally and chemically acetylated polysaccharides: Structural characteristics, synthesis, activities, and applications in the delivery system: A review. *Carbohydrate Polymers, 313*, Article 120746. https://doi.org/10.1016/j.carbpol.2023.120746

Li, N., Qin, H., Tang, Q., Peng, D., Luo, X., Li, H., & Zou, Z. (2024). Development and application of intelligent packaging films based on carboxymethyl starch/PVA with cu-LTE nanocrystal as functional compatibilizer. *Food Packaging and Shelf Life, 43*, Article 101306. https://doi.org/10.1016/j.fpsl.2024.101306

Li, Y., Zhuo, J., Liu, P., Chen, P., Hu, H., Wang, Y., Zhou, S., & Wang, Y. (2018). Distinct wall polymer deconstruction for high biomass digestibility under chemical pretreatment in *Miscanthus* and rice. *Carbohydrate Polymers, 192*, 273–281. https://doi.org/10.1016/j.carbpol.2018.03.013

Liao, G., Sun, E., Kana, E. B. G., Huang, H., Sanusi, I. A., Qu, P., & Shuai, L. (2024). Renewable hemicellulose-based materials for value-added applications. *Carbohydrate Polymers, 341*, Article 122351. https://doi.org/10.1016/j.carbpol.2024.122351

Liao, J., Zhou, Y. H., Hou, B., Zhang, J. M., & Huang, H. H. (2023). Nano-chitin: Preparation strategies and food biopolymer film reinforcement and applications. *Carbohydrate Polymers, 305*, Article 120553. https://doi.org/10.1016/j.carbpol.2023.120553

Ling, Z., Liu, W. Y., Ren, Y. X., Chen, H., Huang, C. X., Lai, C. H., & Yong, Q. (2021). Bioinspired manufacturing of oriented polysaccharides scaffolds for strong, optical haze and anti-UV/bacterial membranes. *Carbohydrate Polymers, 270*, Article 118328. https://doi.org/10.1016/j.carbpol.2021.118328

Liu, G., Shi, K., & Sun, H. (2023). Research progress in hemicellulose-based nanocomposite film as food packaging. *Polymers, 15*(4), Article 979. https://doi.org/10.3390/polym15040979

Liu, H., Feng, Y., Cao, X., Luo, B., & Liu, M. (2021). Chitin nanocrystals as an eco-friendly and strong anisotropic adhesive. *ACS Applied Materials & Interfaces, 13*, 11356–11368. https://doi.org/10.1021/acsami.1c02000

Liu, H., Wang, Z. H., Xin, H. W., Liu, J., Wang, Q. Q., Pang, B., & Zhang, K. (2024). Polysaccharide nanocrystals-based chiral nematic structures: From self-assembly mechanisms, regulation, to applications. *ACS Nano, 18*, 22675–22708. https://doi.org/10.1021/acsnano.4c03130

Liu, Y. Y., Fu, S. M., Jin, K. M., Cheng, Y. G., Li, Y. Q., Zhao, Y. J., & Tian, Y. (2025). Advances in polysaccharide-based conductive hydrogel for flexible electronics. *Carbohydrate Polymers, 348*, Article 122836. https://doi.org/10.1016/j.carbpol.2024.122836

Lv, Z., Rao, J., Lü, B., Chen, G., Hao, X., Guan, Y., & Peng, F. (2023). Microencapsulated phase change material via pickering emulsion based on xylan nanocrystal for thermoregulating application. *Carbohydrate Polymers, 302*, Article 120407. https://doi.org/10.1016/j.carbpol.2022.120407

Ma, Y. S., Morozova, S. M., & Kumacheva, E. (2024). From nature-sourced polysaccharide particles to advanced functional materials. *Advanced Materials, 36*, Article 2312707. https://doi.org/10.1002/adma.202312707

Maingret, V., Courrégelongue, C., Schmitt, V., & Héroguez, V. (2020). Dextran-based nanoparticles to formulate ph-responsive Pickering emulsions: A fully degradable vector at a day scale. *Biomacromolecules, 21*, 5358–5368. https://doi.org/10.1021/acs.biomac.0c01489

Marchessault, R. H., Morehead, F. F., Walter, N. M., Glaudemans, C. P. J., & Timell, T. E. (1961). Morphology of xylan single crystals. *Journal of Polymer Science, 51*. https://doi.org/10.1002/pol.1961.1205115637. Article S66.

Meng, Z., Sawada, D., Laine, C., Ogawa, Y., Virtanen, T., Nishiyama, Y., & Kontturi, E. (2021). Bottom-up construction of xylan nanocrystals in dimethyl sulfoxide. *Biomacromolecules, 22*, 898–906. https://doi.org/10.1021/acs.biomac.0c01600

Naidu, D. S., Hlangothi, S. P., & John, M. J. (2018). Bio-based products from xylan: A review. *Carbohydrate Polymers, 179*, 28–41. https://doi.org/10.1016/j.carbpol.2017.09.064

Peng, L., Hocart, C. H., Redmond, J. W., & Williamson, R. E. (2000). Fractionation of carbohydrates in *Arabidopsis* root cell walls shows that three radial swelling loci are specifically involved in cellulose production. *Planta, 211*, 406–414. https://doi.org/10.1007/s004250000301

Peng, Y., Wei, X., Liang, Y., Wang, X., Chen, S., & Niu, X. (2024). Advances in structural color composite films based on cellulose nanocrystals. *Industrial Crops and Products, 221*, Article 119294. https://doi.org/10.1016/j.indcrop.2024.119294

Qaseem, M. F., Shaheen, H., & Wu, A. M. (2021). Cell wall hemicellulose for sustainable industrial utilization. *Renewable & Sustainable Energy Reviews, 144. Article 110996*. https://doi.org/10.1016/j.rser.2021.110996

Qaseem, M. F., & Wu, A. M. (2020). Balanced xylan acetylation is the key regulator of plant growth and development, and cell wall structure and for industrial utilization. *International Journal of Molecular Sciences, 21*, Article 7875. https://doi.org/10.3390/ijms21217875

Qaseem, M. F., Zhang, W., Dupree, P., & Wu, A.-M. (2024). Xylan structural diversity, biosynthesis, and functional regulation in plants. *International Journal of Biological Macromolecules, 291*. https://doi.org/10.1016/j.ijbiomac.2024.138866. Article 138866.

Rao, J., Lv, Z. W., Chen, G. G., & Peng, F. (2023). Hemicellulose: Structure, chemical modification, and application. *Progress in Polymer Science, 140*, Article 101675. https://doi.org/10.1016/j.progpolymsci.2023.101675

Rennie, E. A., & Scheller, H. V. (2014). Xylan biosynthesis. *Current Opinion in Biotechnology, 26*, 100–107. https://doi.org/10.1016/j.copbio.2013.11.013

Seidi, F., Yazdi, M. K., Jouyandeh, M., Habibzadeh, S., Munir, M. T., Vahabi, H., & Saeb, M. R. (2022). Crystalline polysaccharides: A review. *Carbohydrate Polymers, 275*, Article 118624. https://doi.org/10.1016/j.carbpol.2021.118624

Sergeev, A. A., Naberezhnykh, G. A., Khomenko, V. A., Amosov, A. V., Nepomnyaschiy, A. V., Solov'eva, T. F., & Novikova, O. D. (2022). *In situ*-synthesized cadmium sulfide quantum dots in pore-forming protein and polysaccharide matrices for optical biosensing applications. *Colloids and Surfaces B: Biointerfaces, 217*, Article 112607. https://doi.org/10.1016/j.colsurfb.2022.112607

Shen, Y., Liang, J., Guo, Y.-L., Li, Y., Kuang, H.-X., & Xia, Y.-G. (2021). Ultrafiltration isolation, structures and anti-tumor potentials of two arabinose- and galactose-rich pectins from leaves of *Aralia elata*. *Carbohydrate Polymers, 255*, Article 117326. https://doi.org/10.1016/j.carbpol.2020.117326

Si, Y. X., Luo, H. Z., Zhou, F. S., Bai, X. Y., Han, L., Sun, H. M., & Cha, R. T. (2021). Advances in polysaccharide nanocrystals as pharmaceutical excipients. *Carbohydrate Polymers, 262*, Article 117922. https://doi.org/10.1016/j.carbpol.2021.117922

Smith, P. J., Curry, T. M., Yang, J.-Y., Barnes, W. J., Ziegler, S. J., Mittal, A., … Urbanowicz, B. R. (2022). Enzymatic synthesis of xylan microparticles with tunable morphologies. *ACS Materials Au, 2*, 440–452. https://doi.org/10.1021/acsmaterialsau.2c00006

Song, G. J. (1989). Crystallography of highly substituted galactomannans: Fenugreek and lucerne gums. *Macromolecular Materials and Engineering, 22*, 2641–2644. https://doi.org/10.1021/ma00196a017

Stamenković, O., Siliveru, K., Veljković, V., Banković-Ilić, I., Tasić, M., Ciampitti, I., & Vara Prasad, P. V. (2020). Production of biofuels from sorghum. *Renewable and Sustainable Energy Reviews, 124*, Article 109769, 1364-0321 https://doi.org/10.1016/j.rser.2020.109769.

Torlopov, M. A., Martakov, I. S., Mikhaylov, V. I., Tsvetkov, N. V., & Krivoshapkin, P. V. (2017). Regulation of structure, rheological and surface properties of chitin nanocrystal dispersions. *Carbohydrate Polymers, 174*, 1164–1171. https://doi.org/10.1016/j.carbpol.2017.07.036

von Baeckmann, C., Rubio, G. M. D. M., Kählig, H., Kurzbach, D., Reithofer, M. R., & Kleitz, F. (2021). Evaporation-induced self-assembly of small peptide-conjugated silica nanoparticles. *Angewandte Chemie International Edition, 60*, 22700–22705. https://doi.org/10.1002/anie.202108378

Wang, Q., Niu, W., Feng, S., Liu, J., Liu, H., & Zhu, Q. (2023). Accelerating cellulose nanocrystal assembly into chiral nanostructures. *ACS Nano, 17*, 14283–14308.

Wang, S., & Xiang, Z. (2021). Highly stable Pickering emulsions with Xylan hydrate nanocrystals. *Nanomaterials, 11*, 14283–14308. https://doi.org/10.1021/acsnano.3c03797

Wang, Y., Fan, C., Hu, H., Li, Y., Sun, D., Wang, Y., & Peng, L. (2016). Genetic modification of plant cell walls to enhance biomass yield and biofuel production in bioenergy crops. *Biotechnology Advances, 34*, 997–1017. https://doi.org/10.1016/j.biotechadv.2016.06.001

Wang, Y., Liu, P., Zhang, G., Yang, Q., Lu, J., Xia, T., & Wang, Y. (2021). Cascading of engineered bioenergy plants and fungi sustainable for low-cost bioethanol and high-value biomaterials under green-like biomass processing. *Renewable and Sustainable Energy Reviews, 137*, Article 110586. https://doi.org/10.1016/j.rser.2020.110586

Wu, H., Qin, J., Hua, X., Wang, Z., Zhang, Z., & Zhang, J. (2024). Self-assembly behavior and adhesive performance of imidazolium cation grafted cellulose nanocrystals in confined space. *Carbohydrate Polymers, 336*, Article 122127. https://doi.org/10.1016/j.carbpol.2024.122127

Wu, H. L., Williams, G. R., Wu, J. Z., Wu, J. R., Niu, S. W., Li, H. Y., & Zhu, L. M. (2018). Regenerated chitin fibers reinforced with bacterial cellulose nanocrystals as suture biomaterials. *Carbohydrate Polymers, 180*, 304–313. https://doi.org/10.1016/j.carbpol.2017.10.022

Xue, X. F., Song, G. J., & Chang, C. Y. (2022). Tough all-polysaccharide hydrogels with uniaxially/planarly oriented structure. *Carbohydrate Polymers, 288*, Article 119376. https://doi.org/10.1016/j.carbpol.2022.119376

Yilmaz-Turan, S., Jiménez-Quero, A., Menzel, C., de Carvalho, D. M., Lindström, M. E., & Vilaplana, F. (2020). Bio-based films from wheat bran feruloylated arabinoxylan: Effect of extraction technique, acetylation and feruloylation. *Carbohydrate Polymers*. , Article 116916. https://doi.org/10.1016/j.carbpol.2020.116916

Zhang, H., Johnson, A. M., Hua, Q., Wu, J., Liang, Y., Karaaslan, M. A., & Renneckar, S. (2023). Size-controlled synthesis of xylan micro / nanoparticles by self-assembly of alkali-extracted xylan. *Carbohydrate Polymers, 315*, Article 120944. https://doi.org/10.1016/j.carbpol.2023.120944

Zhang, H., Yu, F., Xie, P., Sun, S., Qiao, X., Tang, S., & Xie, Q. (2023). A Gγ protein regulates alkaline sensitivity in crops. *Science, 379*. https://doi.org/10.1126/science.ade8416

Zhang, R., Hu, Z., Peng, H., Liu, P., Wang, Y., Li, J., & Peng, L. (2023). High density cellulose nanofibril assembly leads to upgraded enzymatic and chemical catalysis of fermentable sugars, cellulose nanocrystals and cellulase production by precisely engineering cellulose synthase complexes. *Green Chemistry, 25*, 1096–1106. https://doi.org/10.1039/D2GC03744K

Zhang, W. T., Zhang, G. R., Lu, X. A., Wang, J., & Wu, D. F. (2021). Cellulosic nanofibers filled poly (*β*-hydroxybutyrate): Relations between viscoelasticity of composites and aspect ratios of nanofibers. *Carbohydrate Polymers, 265*, Article 118093. https://doi.org/10.1016/j.carbpol.2021.118093

Zhang, Y., Wang, L., Zhang, H., Rosqvist, E., Lastusaari, M., Peltonen, J., & Pranovich, A. (2024). Crystalline nanoxylan from hot water extracted wood xylan at multi-length scale: Molecular assembly from nanocluster hydrocolloids to submicron spheroids. *Carbohydrate Polymers, 335*, Article 122089. https://doi.org/10.1016/j.carbpol.2024.122089

Zhu, Y., Ju, Z., Zhang, X., Lutz, D. M., Housel, L. M., Zhou, Y., & Yu, G. (2020). Evaporation-induced vertical alignment enabling directional ion transport in a 2D-nanosheet-based battery electrode. *Advanced Materials, 32*(10). https://doi.org/10.1002/adma.201907941